The prediction of crack propagation in coarse grain RR1000 using a unified modelling approach

B. Engel [a], J. P. Rouse [a], C. J. Hyde [a], W. Lavie [a], D. Leidermark [b], S. Stekovic [b], S. J. Williams [c], S. J. Pattison [c], B. Grant [c], M. T. Whittaker [d], J. P. Jones [d], R. J. Lancaster [d] and H.Y Li [e].

[a] Gas Turbines & Transmissions Research Centre, Faculty of Engineering, University of Nottingham, Nottingham, United Kingdom, NG8 1BB,
[b] Department of Management and Engineering, Linköping University, Linköping , Sweden, SE-581 83,
[c] Rolls-Royce plc., Derby, United Kingdom DE24 9GJ,
[d] College of Engineering, Swansea University, Swansea, United Kingdom, SA1 8EN,
[e] School of Metallurgy and Materials, University of Birmingham, Birmingham, United Kingdom, B15 2SE.

Corresponding Author: benedikt.engel@nottingham.ac.uk

Abstract

The polycrystalline nickel-base superalloy RR1000 is used as turbine rotor material in Rolls-Royce aero engines and has to withstand a wide variety of load and temperature changes during operation. In order to maximize the potential of the material and to improve component design, it is of great interest to understand, and subsequently be able to accurately model the crack propagation caused by thermo-mechanical fatigue conditions. In this work, experimental data is analysed and used to inform unified modelling approaches in order to predict the crack propagation behaviour of RR1000 under a variety of stress-controlled thermo-mechanical fatigue conditions.

1. Introduction

Components located within the hot gas section of gas turbines for aircraft application, undergo numerous start-stop procedures, as well as load and temperature changes during their lifetime. The resulting alternating mechanical and thermal loads can lead to crack formation within critical areas and finally to fatal damage to the component. Turbine rotors made of polycrystalline nickel-base superalloys are particularly crucial to the operational safety and service life of gas turbines and accordingly are classed as critical parts which mandates rigorous adherence to stringent safety criteria. To extend the range of applicability of these assessments, it is important to understand the crack initiation and propagation behaviour under thermo-mechanical fatigue (TMF) loading. Since experimental investigation of crack initiation and propagation under TMF loading is expensive and time consuming, unified models are indispensable in order to predict the material behaviour during the design process.

In general, the material behaviour, i.e. the crack growth behaviour under high temperature or thermo-mechanical fatigue is a complex mechanism which depends on a large number of factors, especially high temperature time dependent effects, such as creep and oxidisation. In contrast to high cycle fatigue tests, where the lifetime is predominantly determined by the crack initiation process, the lifetime under high temperature low cycle fatigue or thermo-mechanical fatigue is dominated by crack propagation. To predict this behaviour with sufficiently high accuracy, it is essential to describe the crack propagation behaviour under the influence of time dependent factors with good accordance to experimental results.

First analytical and empirical descriptions of crack growth were done by Paris and Erdogan [1], where the crack growth rate is described by a power law function in dependence of stress intensity factor, K, where C and m are material constants. The stress intensity factor, introduced by George R. Irwin in 1957 [2], represents the stress field in front of the crack tip under the assumption of a homogeneous and elastic material behaviour. To generate a linear crack propagation (long crack growth) according to the Paris law, the cyclic stress intensity factor range, ΔK, has to exceed a threshold value, ΔK_{th}, which is a material constant. As Forman in [3] mentioned, the Paris law doesn't seem complete, due to not taking into account two important effects. One is the influence of different R-ratio on the crack growth as studied by several authors [4–6]. With the introduction of a modified Paris law with an exponential function taking into account the load ratio R, a description of crack growth in aluminium plates under different load ratios was possible as shown by Broek et al [7]. Second is the not accountable instable crack growth after the stress intensity factor exceeds the critical stress intensity factor K_{crit}. With the proposed modification of the Paris law in the Forman model, both effects can be represented as shown by equation 1 (with C and n as material parameters).

$$\frac{da}{dN} = \frac{C(\Delta \mathrm{K})^{n}}{(1-R)(K_{crit}-\Delta \mathrm{K})} \tag{1}$$

A large number of works of the last decades prove the applicability of the Forman model and its variations for numerous materials like aluminium and steels [8,9].

However, only time independent effects can be predicted using the mentioned formulation. In order to model time dependent effects such as creep as well as oxidation on the crack growth of nickel-base superalloy under high temperature conditions, Tong et al [10] proposed a single term variation of the Paris law. Modifying the exponents and implementing an Arrhenius relationship, they were able to predict the crack growth in the nickel-base superalloy U720Li under different loading waveforms at 650 °C and R = 0.1.

Another approach is to model the creep crack growth and fatigue crack growth separately, where the sum of both leads to the total crack growth, as proposed by Kruch et al [11]. This method was developed to predict the fatigue and creep crack growth under complex cyclic loading for the polycrystalline nickel-base superalloy Astroloy at 650 °C. In addition, the model consolidates environmental effects, such as oxidization at the crack tip with a resulting embrittlement of the material and therefore a reduction in mechanical properties. As a result, the crack growth rate increases which can be modelled through a variation of the local toughness K_C.

Wolf et al. improved the evaluation of crack growth rate by introducing the crack closure phenomena in the calculation of $\frac{da}{dN}$ [12]. Due to the formation of a plastic zone in front of the crack tip during cyclic testing, the crack can be closed even under tensile loading, which results in a decrease of ΔK . Since crack growth only occurs for opened cracks, the effective stress intensity factor ΔK_{eff} can be calculated by the difference between the maximum stress intensity factor ΔK_{max} and the stress intensity factor ΔK_{op} when the crack starts to open. Using the crack closure approach, Arana et al. [13] predicted the crack growth rate for the single crystal material SRR99 under TMF conditions using a modified Paris law with additional oxidisations effects. In addition to the previously mentioned plastically induced crack closure; oxidized, corroded or roughened crack flanks can lead to crack closure effects [14–17]. Further phase transformations induced by plastic deformation in the area of the crack tip can also cause crack closure effects [17,18]. A detailed description and explanation of the mechanism of crack closure effects can be found in [19]. In many modelling works, phenomenological models based on modified versions of the Paris law (i.e. Forman model) were used with good accordance to the experimental tests. All models for the crack growth behaviour mentioned in the section above can be attributed to linear elastic fracture mechanics. The material behaviour in front of the crack tip can be calculated using elastic material laws and are applicable as long as the plastic zone of the crack tip is comparatively small. Due to the elastic calculation, a stress singularity at the crack tip evolves, leading in reality, to a plastic deformation as the yield strength is exceeded. Parameter which describe the plastic deformation in front of the crack tip are crack tip opening displacement ($\Delta CTOD$) as well as the J-integral [20,21]. A linear elastic approach is employed within this work for the description of the crack growth modelling under TMF conditions.

2. Material and Modelling

2. 1 Investigated Material and Experimental Setup

The investigated material is the polycrystalline nickel-base superalloy RR1000, developed by Rolls-Royce plc. It is a γ' precipitation strengthened powder processed material for high temperature applications with the following composition shown in Table 1.

Table 1: Composition of RR1000 in wt.%

Ni	Cr	Co	Mo	Al	Ti	Ta	Hf	Zr	C	B
Bal.	15	18.5	5	3	3.6	2	0.5	0.06	0.027	0.015

After a complex multi-step heat treatment, the microstructure consists of finely dispersed and uniformly distributed secondary and tertiary γ' particles. Typical sizes for the secondary γ' are 50-350 μm and for the tertiary γ' 5-50 μm. Furthermore, grain sizes of about 50 μm for the coarse grained version and 7 μm for the fine grained RR1000 are commonly found [22]. Volume fraction and size distribution of the precipitates are mainly responsible for the excellent mechanical properties of this material at high temperatures [23,24].

Experimental tests were carried out at SMaRT (Swansea Materials Research & Testing ltd.) at Swansea University with specimens taken from a rotor component before the main TMF testing. Corner notched test specimens with a 7 mm square cross section and a gauge length of 20 mm, were pre-cracked at room temperature to an average crack length of 1 mm. Following this, stress controlled TMF crack growth tests were conducted using a servo hydraulic test rig with an induction coil heating system. During pre-cracking and TMF testing, crack growth was measured using direct current potential drop (DCPD) signals. Further information about the experimental setup can be found in [25].

2. 2 Crack growth modelling under complex thermo-mechanical loading

For long crack propagation simulations under complex thermo-mechanical loading, the work of Bouvard et al. on Nickel-based AM1 will be used as a basis in the following work [26]. Bouvard et al's investigations were carried out for a single crystal nickel-base superalloy, but it is mentioned, that the model is also applicable for polycrystalline nickel-base superalloys [11,26]. As a starting point, the long crack growth rate is decomposed linearly into two parts, fatigue and creep, and encouragement of crack growth given in equation 2.

$$da = (\frac{da}{dN})_{fatigue} dN + (\frac{da}{dt})_{creep} dt \tag{2}$$

According to eq. 2, the crack growth rates can be calculated individually for each mechanism ($(\frac{da}{dN})_{fatigue}$ and $(\frac{da}{dt})_{creep}$, respectively) and the total crack extension da estimated using the applied number of cycles dN and the exposure time dt. For isothermal applications, the stress intensity factor can be assumed to be constant. But considering the changes in stress intensity factor in dependence of the temperature $T(t)$ for a single cycle during thermo-mechanical fatigue loading, a reduced stress $S(t)$ is introduced according to eq. 3, with $K(t)$ as current stress intensity factor. To assure convergence during the calculation, the loading has to be discretized into small time steps, to pay respect to the temperature evolution during thermo-mechanical loading.

$$S(t) = \frac{K(t)}{K_{cv}(T(t))} \tag{3}$$

$K_{cv}(T(t))$ is the temperature and time dependent material toughness (of the virgin material) under conditions where oxidisation effects are negligible. The temperature dependence of $K_{cv}(T(t))$ is modelled using an Arrhenius type function to modify a reference value K_{cv}^0 , where Q is an activation energy, k_R is the universal gas constant and η_f^* is a temperature independent material parameter.

$$K_{cv}(T(t)) = K_{cv}^0 \exp\left(\frac{Q}{(\eta_f^* - 1)k_R T(t)} \right) \tag{4}$$

With the usage of the Forman model [3] the fatigue crack propagation $\frac{da}{dN}$ can be rewritten with the definitions above (using eq. 2 and 3).

$$\frac{da}{dN} = \frac{C_f^* (\Delta S)^{\eta_f^*}}{(1-R)(S_C - S_M)} \tag{5}$$

C_f^* and η_f^* are material parameters. ΔS is in analogy to the Forman model (see equation (1)) the normalized effective temperature dependent stress intensity range.

$$\Delta S = S_M - S_s^f = \frac{K_M - K_s^f}{K_{cv}(T(t))} \tag{6}$$

K_s^f represents the temperature independent fatigue crack growth resistance and K_M the maximum stress intensity factor during the investigated cycle. It should be noted here that the creep crack growth component within the present modelling approach is taken to be the difference between the total crack growth at high temperature and the fatigue crack growth contribution. As experimental results of isothermal crack growth testing for a wide range of temperature reveals, the total crack growth at high temperature is significantly increased when compared to tests at lower temperatures and can’t be described only by fatigue crack growth effects. Time dependent test data provided by Rolls-Royce plc. shows that, beyond a critical temperature, creep effects are evident. Therefore it can be assumed that in both, isothermal and high peak temperature an-isothermal fatigue crack growth testing, creep effects at the crack tip are induced. Due to no/low holding times during cycling for the proposed experiments, as well as the localised creep effects at the crack tip (no creep deformation of the bulk material is expected), experimental observation using bulk displacement measurements is not sufficient. The proposed creep modelling approach is not, therefore, based on displacement data. For the evaluation of the creep crack growth contribution to the total crack growth, equation 7 is used in accordance to [11].

$$da = C_C\big(T(t)\big)\big(K(t) - K_S^C\big)^{\eta_C(T(t))} dt \tag{7}$$

As equation 7 reveals, K was chosen as a parameter to describe the creep crack growth due to the following reasons (according to [26]): The C*-integral or the J-integral, which are also valid parameters to describe creep crack growth, are usually applied to ductile materials as well as for stationary creep conditions. However, due to the investigated material and the cyclic occurrence of creep effects at the crack tip caused by the testing, they are not suitable for the current approach.

Furthermore, the successful application of K for describing the creep crack growth under an-isothermal test condition, could be shown for nickel-base superalloys in [11,26].

$C_C\big(T(t)\big)$ and $\eta_C\big(T(t)\big)$ are both temperature dependent material parameters and have to be updated stepwise during the cycle. Since all experimental tests were conducted for the same stress rate as well as waveform of the practical application, it was considered unnecessary to model rate dependent creep effects. In order to consider creep and fatigue interaction, the following relaxation type evolution equation is used in order to reduce the fatigue threshold value K_s^f:

$$D\left(\frac{K_s^f}{K(t)}\right) = -A\big(T(t)\big)\left(\frac{K_s^f}{K(t)}\right)^{\omega(T(t))} dt \tag{8}$$

Where $A\big(T(t)\big)$ and $\omega\big(T(t)\big)$ are temperature dependent material parameters.

2. 3 Determination of material parameters

Model parameters were derived using isothermal crack growth experimental data provided by Rolls Royce plc. A multitude of isothermal crack growth tests for different R-ratios and for a temperature range from 20 °C to 800 °C in air as well in vacuum were analysed. By partitioning data into high and low temperature sub sets creep crack growth mechanisms can be considered accounted for or neglected, respectively. Furthermore, in vacuum tests are considered in isolation to in air tests, allowing for the effects of oxidisation on crack growth rates to be approximated. These simple data partitioning approaches greatly simplify the material parameter determination process and form a tractable problem. The fatigue parameters ($K_{cv}^0, \eta_f^*, C_f^*, Q$ and K_s^f) were first determined from tests performed in conditions where creep and oxidization effects could be neglected (i.e. low temperature and in vacuum conditions). Initial estimations were made by taking logarithms of equation (5) and approximating experimental crack growth data with the resulting (assumed) linear fit. Note that temperature independent fatigue resistance values, K_s^f, were estimated directly from experimental data by observing the stress intensity factor values required in order to initiate cracking at the start of the test. Estimates of the fatigue crack growth model parameters are made for each low temperature experimental data set independently. K_{cv} is therefore assumed as a constant for each test temperature, with the temperature dependent function expressed in equation (4) being fitted to these to determine the relevant parameters. Estimates of fatigue parameters are then averaged over all low temperature data sets to produce a set of initial estimates of $K_{cv}^0, \eta_f^*, C_f^*, Q$ and K_s^f. The creep parameters K_S^C, C_C, η_C, A and ω were extracted from high temperature tests in vacuum. In order to determine the pure creep behaviour, estimates of $\left(\frac{da}{dN}\right)_{fatigue}$ were evaluated (using the initial estimates of $K_{cv}^0, \eta_f^*, C_f^*, Q$ and K_s^f discussed above) and subtracted from the total crack growth rate $\left(\frac{da}{dN}\right)_{total}$. A logarithmic form of equation (7) is then taken and used to fit estimates of K_S^C, C_C, η_C, A and ω to $\left(\frac{da}{dN}\right)_{creep}$ for each high temperature in vacuum condition. In the case of temperature independent parameters (K_S^C, C_C, and η_C) these were averaged for all test conditions to produce a set of initial estimates. In the case of A and ω averaging was performed on a temperature by temperature basis, thereby allowing simple (exponential form) temperature dependent functions to be fitted to the data. Initial estimates of the 9 material parameters were then optimised using the Matlab function LSQNONLIN by evaluating the difference between predicted and experimental crack growth rates for all test conditions for a range of loads. Objective functions therefore take a simple sum of squares form, with weighting functions being applied to these values in order to limit the bias to experimental data sets with more data points. Creep crack growth mechanism were manually excluded in low temperature predictions by defining a creep activation temperature. It should be noted that all crack growth rates in the following figures are normalised on the basis of confidential data (marked by "norm.").

2. 4 Influence of oxidisation

As it will be later shown and discussed in section 3.3, the crack growth within this material at high temperatures strongly depends on the microstructure. Therefore, for tests in air, it is not easy to determine the separate influences of microstructure and oxidation on the crack growth behaviour. Figure 1 shows a comparison of isothermal crack growth tests in air and in vacuum at 750 °C for a one second ramp followed by one second of holding time (noted as 1-1-1-1, see diagram) waveform for two different R-ratios.

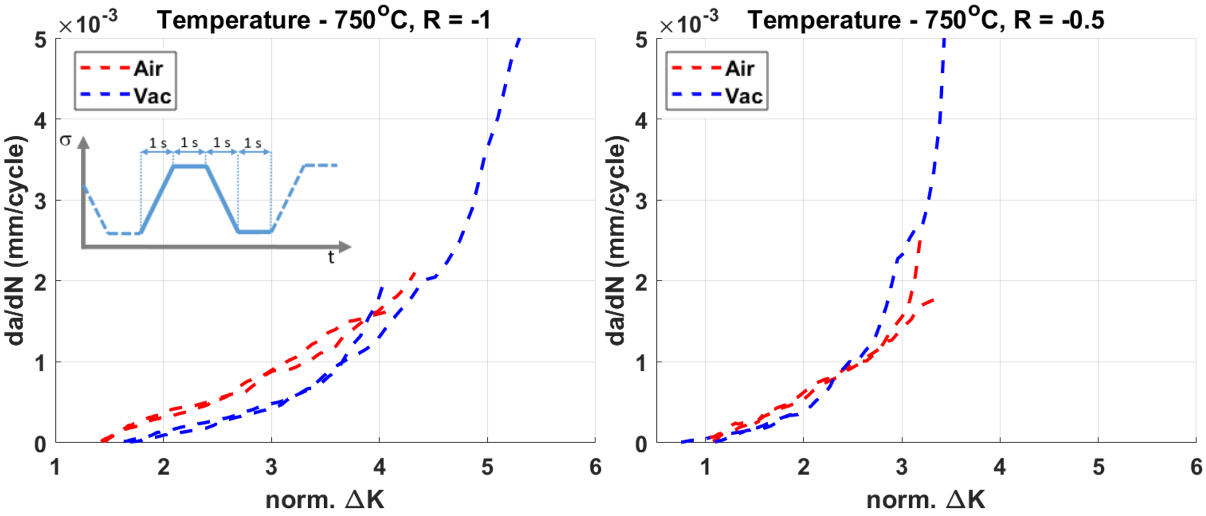

Figure 1: Crack growth rates for isothermal LCF tests at 750 °C in air and vacuum for R = -1 (left) and for R = -0.5 (right).

Both figures with different R-ratios show a slight increased crack growth rate for tests in air. Based on limited available data, it cannot be stated, that crack growth for these tests is enhanced due to oxidation. The variation could also arise from varying microstructure, resulting in variable crack growth rates. This is supported by the fact that a distinct scatter in the crack growth can be also observed in the following vacuum tests (see Figure 2), which were conducted with a 1-1-1-1 waveform at 550 °C and 600 °C.

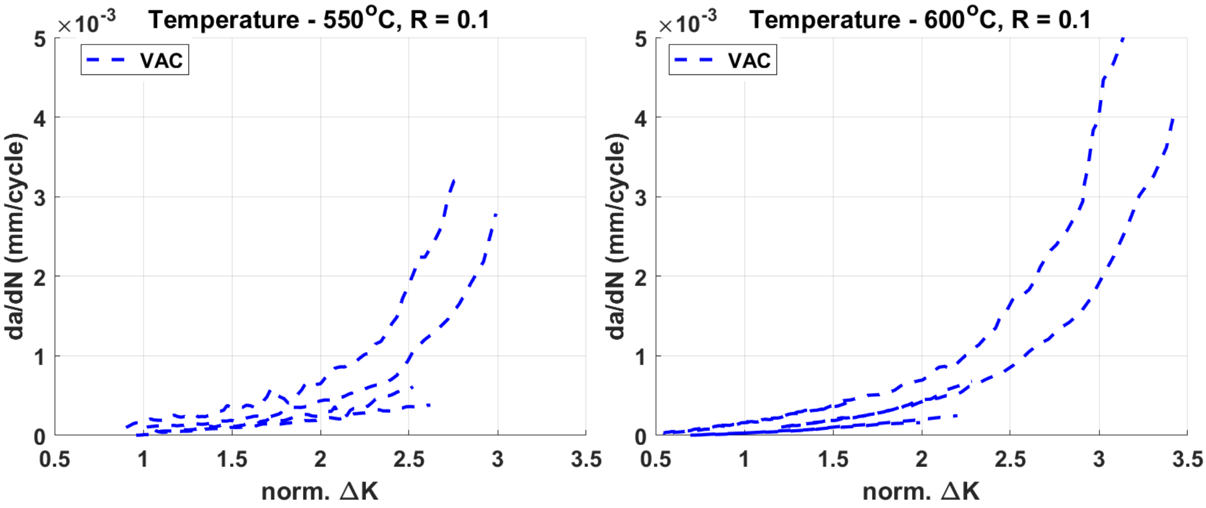

Figure 2: Isothermal crack growth tests in vacuum for the temperatures 550 °C (left) and 600 °C (right).

Due to the lack of data, as well as the above mentioned complexity of the dissection of the different effects no oxidation effects could be considered in the current state of the model. For future model developments oxidation tests will be conducted, to model the reliable influence of oxygen on the crack growth behaviour in independence of microstructural scatter.

3. Results & Discussion

In the following section, the results of the modelling work compared to the experimental determined crack growth behaviour are presented. Section 3.1 focusses on the prediction of isothermal tests, as the material parameters have been evaluated from these tests. Crack growth tests under TMF conditions i.e. under varying temperatures during cycling, were predicted using these parameters and are presented in section 3.2.

3.1 Prediction of isothermal Data

Figure 3 shows the prediction of the crack growth rate for two tests with same test conditions, at 200 °C and a load ratio of R = - 0.5. These tests were conducted in air atmosphere (Air).

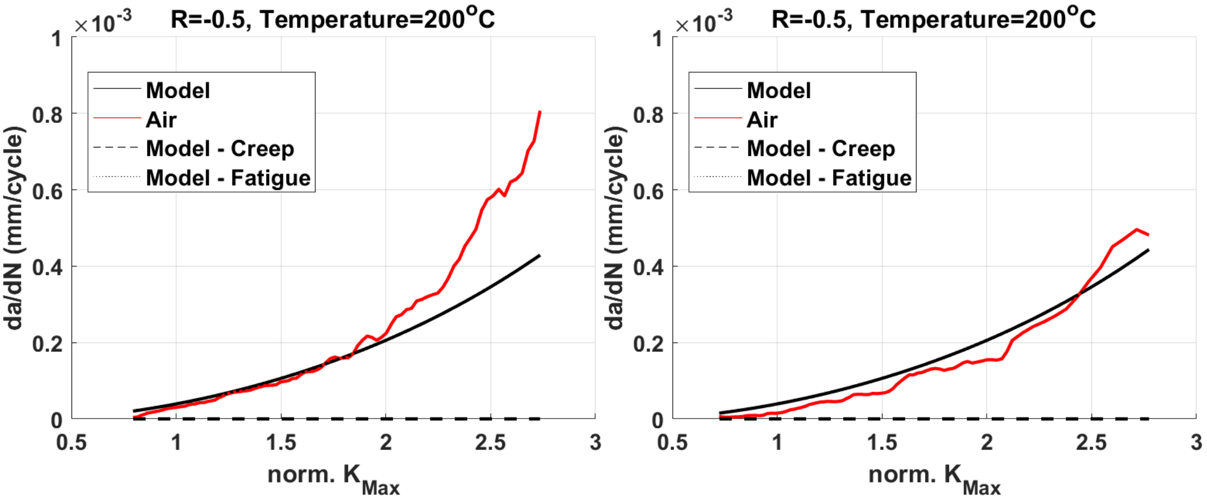

Figure 3: Prediction of crack growth rates in two tests for isothermal testing at 200 °C.

The predicted values (Model) for the crack growth show a good accordance to the experimental test data. Since the test conditions are exactly the same, the predicted crack growth rates are similar, and deviations result from scatter in the experimental results. Due to the test temperature of 200 °C, the effects of creep can be neglected, and the long crack propagation is dominated by fatigue. In these circumstances the predicted fatigue crack growth is equal to the total crack growth. Figure 4 shows the isothermal crack growth behaviour for two tests and a load ratio, R = 0.1 (in air) and 650 °C, where creep crack growth can be expected.

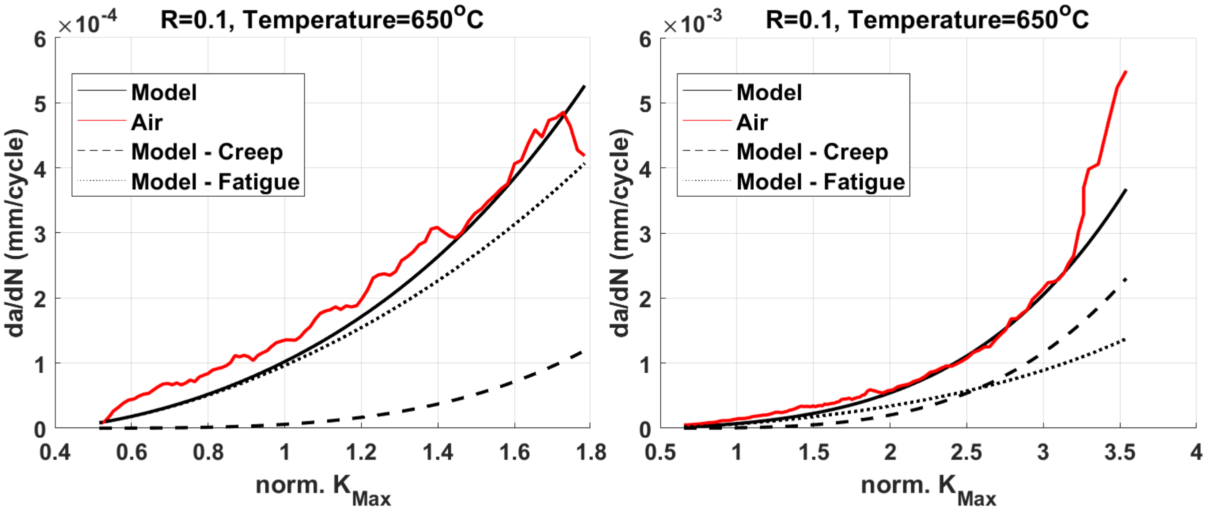

Figure 4: Prediction of crack growth rates for two isothermal tests at 650 °C for norm. K_{Max} below 1.8 (left) and below 3.5 (right).

The model can also predict isothermal crack growth rates with good accordance for temperatures up to 650 °C as shown in Figure 4. It turns out, that especially for normalized stress intensity factors above 1 a clear influence of creep crack growth occurs. Below 2.5 crack growth is almost fully driven by fatigue crack growth. For normalized stress intensity factors above 2.5 creep becomes more dominant than the fatigue crack growth. Note that both tests were conducted under the same test conditions, but the test in Figure 4 right was stopped close to a critical stress intensity factor. Due to distinct longer test time the scales of the axis are not equal.

3.2 Prediction of an-isothermal Data

Based on the parameters determined from isothermal tests shown and described in 3.1, an-isothermal tests were predicted. TMF tests with phase shifts of 0° (in-phase, IP) and 180 ° (out-of-phase, OP) in temperature and stress were predicted and compared to experimental tests. Figure 5, shows the prediction for two out-of-phase tests between 400 °C and 750 °C, in air for a load ratio of R = 0.

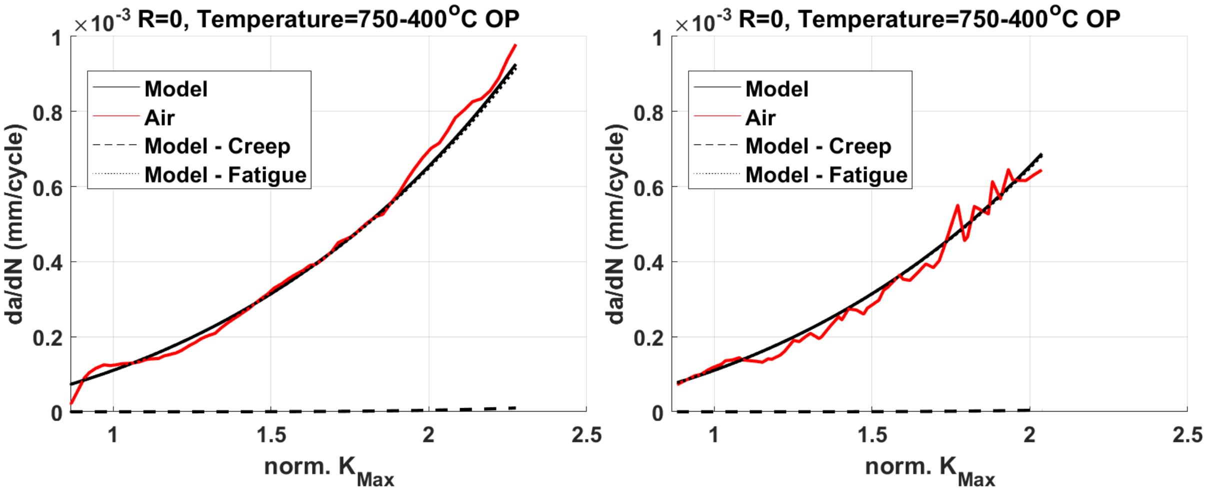

Figure 5: Prediction of crack growth rates for two OP-TMF tests at 400 °C -750 °C in air.

The application of the model for an-isothermal crack growth prediction shows very good agreement with the experimental results for out-of-phase tests. As it can be determined from the numerical results, the crack growth behaviour is significantly driven by fatigue crack growth. For this reason, the prediction of fatigue crack growth and the total crack growth practically align. A detailed data analysis of the prediction data indicates creep crack growth over the whole test, but with a magnitude more than 300 times smaller compared to the fatigue crack growth. Figure 6 shows the development of the stress intensity factor and the development of the creep crack growth (CG) rate for the last cycle of an OP TMF test between 400 °C and 750 °C.

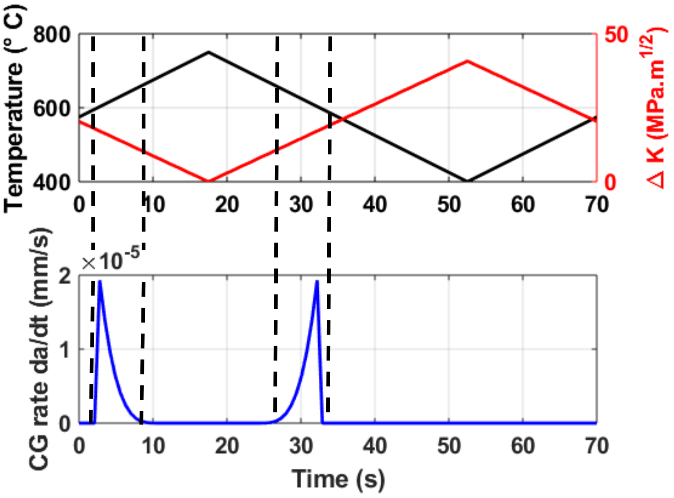

Figure 6: Development of creep crack growth for the last cycle of an OP TMF test.

As expected, creep crack growth only occurs in the high temperature part of the loading cycle. Because of the OP testing procedure, temperature increases while the applied stress decreases, therefore only in a small window, where the temperature and stress intensity factor are high enough, does creep crack growth occur. The dominance of fatigue crack growth can also be explained by the phase angle during OP TMF testing. Crack growth only occurs at open cracks while the crack tip exceeds a critical value of stress intensity factor. For out of phase testing at maximum stress the temperature minimum is reached and therefore there is no creep influence on the crack propagation. In contrast, in-phase tests where at maximum stress (i.e. crack opening) the maximum temperature prevails; crack growth is highly influenced by creep mechanisms. Figure 7 shows the prediction of the crack growth for two in-phase TMF tests between 400 °C and 750 °C.

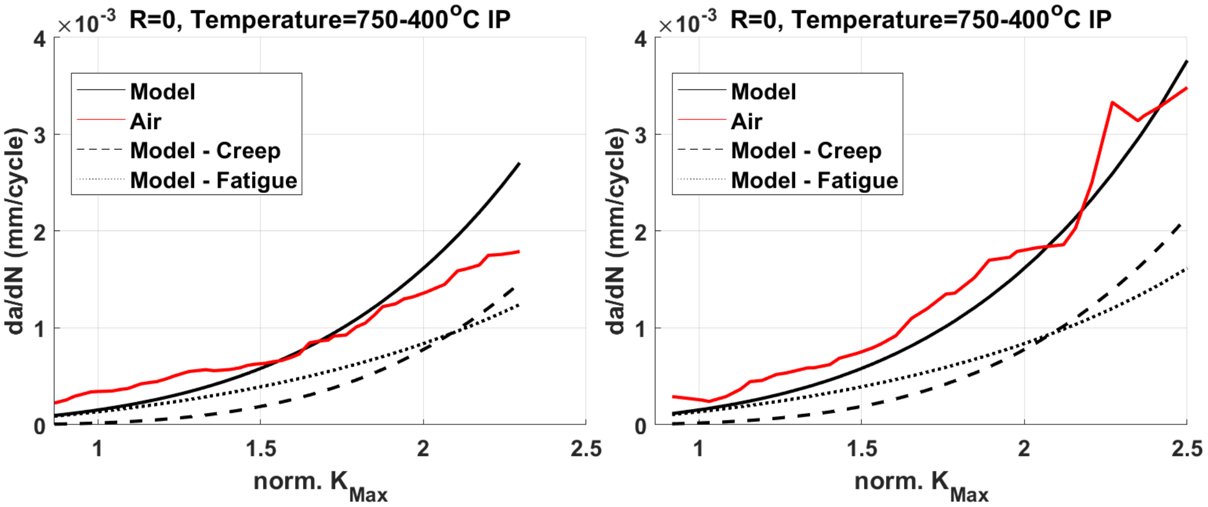

Figure 7: Prediction of crack growth rates for two IP-TMF tests at 400 °C -750 °C in air.

The model is also able to predict the shown in-phase tests with acceptable accordance to the experimental results. Creep crack growth already occurs at low maximum normalized stress intensity factors > 1. Up to a normalized stress intensity factor of 2.2 creep crack growth overtakes the fatigue crack growth and becomes the dominant mechanism. This significantly increased creep is caused by high temperatures compared with high stresses i.e. stress intensity factors during IP testing. The following Figure 8 shows the evolution of creep crack growth during the last cycle of an IP test between 400 °C and 750 °C.

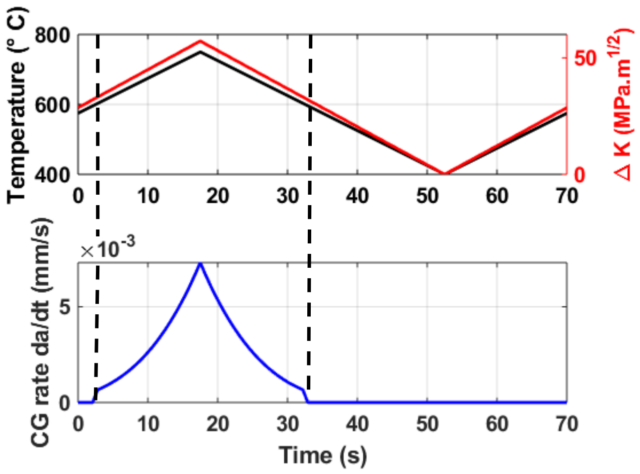

Figure 8: Development of creep crack growth for the last cycle of an IP TMF test.

Figure 8 shows that creep crack growth occurs nearly during half of the TMF cycle as soon as the critical creep activation temperature of 600 °C is reached. During increasing temperature, the stress intensity factor also increases, which results in significantly higher creep crack growth rates, compared to the OP TMF tests. Due to the current model formulation it is not possible to simulate the fatigue crack propagation during a single cycle since equation 4 already calculates the total da/dN.

3.3 General model application to an-isothermal TMF tests

The following Figure 9 compares the predictions of OP and IP tests (OP, IP Pred) with all performed experimental tests (OP, IP Exp) in order to prove the general applicability of the model.

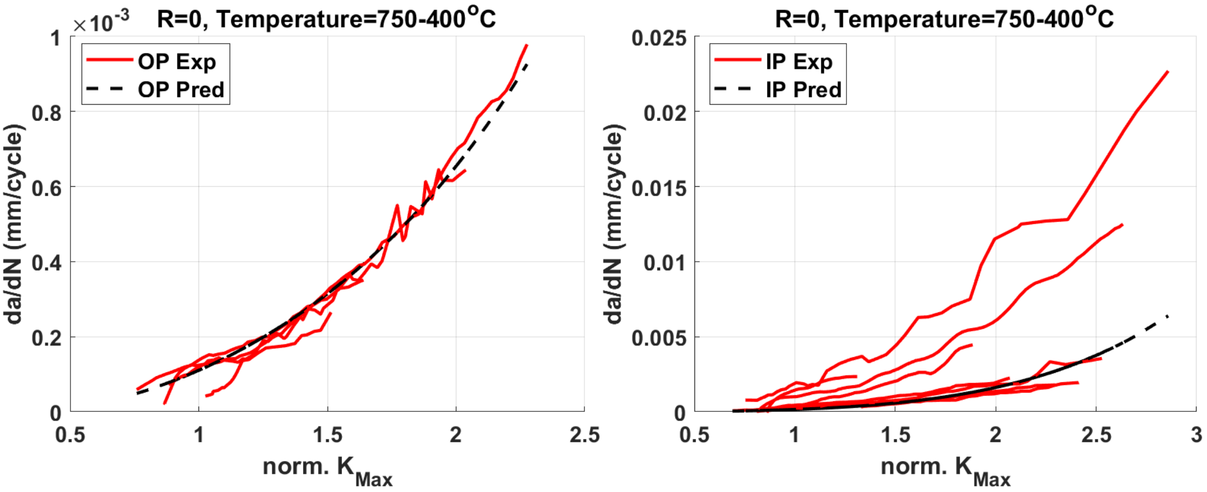

Figure 9: Summary of OP (left) and IP (right) TMF tests prediction for temperatures from 400 °C – 750 °C compared to experimental data.

The low scatter in the experimental data for the OP tests, allows a very good prediction with high accordance to the test data as Figure 9 (left) shows. However, the experimental results for the IP tests indicate significant scatter for the crack growth behaviour for similar test conditions. The current state of the model is just able to capture the lower boundary region of the conducted IP tests. Microstructural evaluation conducted by John et al [25] showed a relationship between decreasing secondary γ' size distribution and increasing crack growth rate under IP-TMF loading for RR1000. In addition, Li et al [27] showed the influence of the microstructure, especially tertiary γ' for isothermal crack growth tests with different hold times. Regarding the experimental data as well as the numerical results, a change in mechanism in plastic deformation and resulting crack growth must occur at peak temperature, where the microstructure must have a significant influence at high temperatures. High temperature deformation tests on in RR1000 were conducted by several researchers [28–30] for a temperature range between 20 °C and 750 °C and analysed by scanning electron and transmission electron microscopy. For temperatures of 20 °C and 500 °C, shearing of the γ' particles can still be found. But the dislocation density in the γ matrix is significantly higher compared to the precipitates, which explains less localised shear deformation in the microstructure. In addition, dislocation pile ups can be found around the particles. For 750 °C an additional dislocation pile up on the interfaces can be found, which lead to a strong bowing around the precipitates. Furthermore, at 750 °C, a large number of stacking faults can be found to be confined by the γ' precipitates only for the coarse γ' precipitates with an average diameter of 232 ± 99 μm. After [31] the stacking faults indicate a change in the nature of the dislocations. For smaller γ' precipitates no stacking faults could be found. It should be noted that the investigations mentioned above [28,29] were carried out for unimodal γ' distributions, where the smallest γ' size was 85 ± 34 mm.

In general, the shearing of particles by dislocations in coherent γ' strengthen nickel-base superalloys occurs by dislocation pairs as proven in [32]. In dependence of the volume fraction and particle size of the alloy, weakly or strongly coupled dislocations pairs are responsible for shearing [33]. For the nickel-base superalloy Udimet720Li with a volume fraction of 50 % the transition from weakly to strongly coupled dislocation shearing occurs for a precipitation size between 45 – 50 μm [34]. For weakly coupled dislocations, the shear stress, which is necessary for shearing, increases with particle size. For strongly coupled dislocations, the shear stress decreases for precipitations sizes > 50 µm. For the investigated specimen within this paper, the material consists of a bimodal distribution of secondary γ' and tertiary γ', therefore a mixture of shearing mechanism occurs. As shown in [35,36], the average yield strength (≈ critical resolved shear stress) can be calculated by superimposing of both effects and a weighting factor which describes the specific strength of the single phases.

The following section focuses on the microstructural characteristics of the investigated material by means of scanning electron microscope (SEM) images. Figure 10 shows such microstructural images of two IP TMF test specimens (TC004 and TC010) close to the crack path after specimen failure.

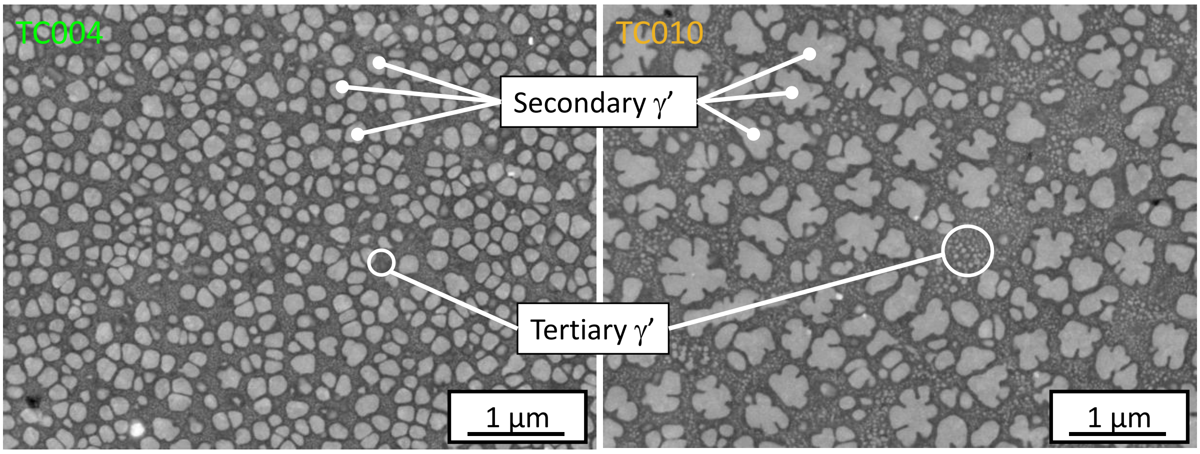

Figure 10: Microstructure of IP TMF tests TC004 (left) and TC010 (right).

The microstructure of these two test specimens show significant differences in terms of size and shape of the secondary γ'. For test specimen TC004 the secondary γ' is more spherical shaped and seems more homogenously distributed in comparison to TC010. The secondary γ' in TC010 is more coarse and in "cloverleaf" shape. According to [37], these cloverleaf shapes evolve during the solidification at low cooling rates, whereas faster cooling rates lead to the more spherical shapes as seen in TC004. The shape of the tertiary $\gamma'$is spherical for both specimens investigated and homogenously embedded within the γ matrix. In TC010, the tertiary γ' appears slightly coarser in comparison to TC004. The differences found in the microstructure can be explained by the extraction of the material from a rotor component. During manufacturing and especially heat treatment, different cooling conditions occur in dependence of the component geometry and therefore different precipitation sizes and distributions can be found within the material [24]. To investigate the precipitates in detail, a field emission gun SEM was used in order to generate images with magnifications between 30k – 80k. The captured images were examined using the software ImageJ to evaluate the size distributions of the precipitates. Details to the specimen preparation technique and the subsequent analyses can be found in [27]. Figure 11 shows the total count of secondary γ' and tertiary γ' and the size distribution for four microstructural investigated IP TMF crack growth tests, all evaluated for a measurement field of 6 x 4.5 µm.

After Jackson [34], the critical size to identify tertiary and secondary precipitates can be specified at 90 µm. In addition, the transition between weakly and strongly coupled dislocation are given at 50 µm. Test TC026 shows the highest, TC010 the lowest crack growth rates under the same IP TMF test conditions [25] (see Figure 13).

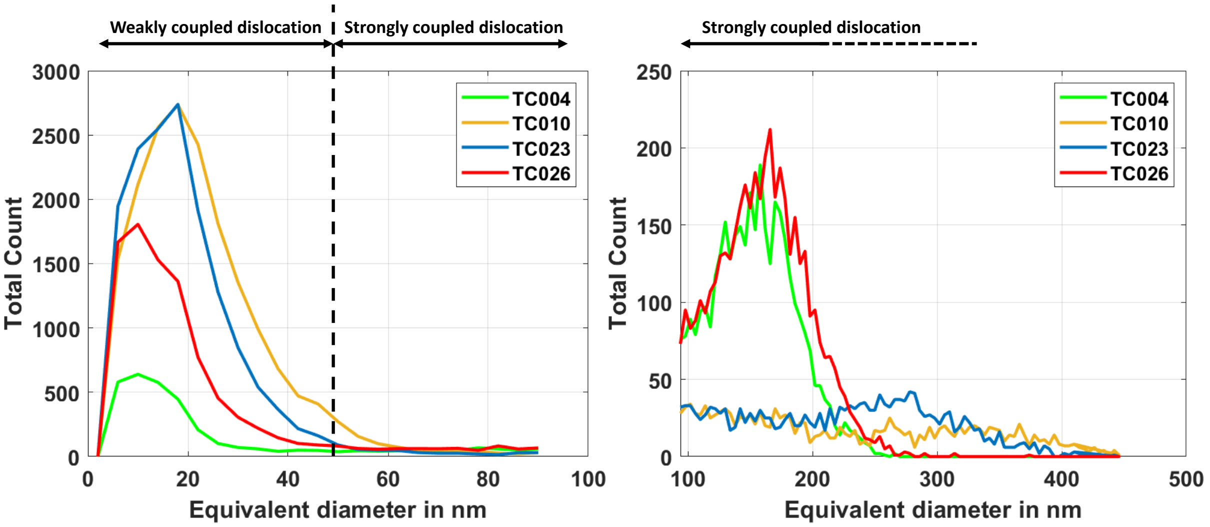

Figure 11: Size distribution of tertiary γ'particles (left) and size distribution of secondary γ'particles (right)

It is clear from Figure 11 that the number of tertiary γ' is significantly higher than the number of secondary γ' for the investigated microstructures. Comparing the results of the distribution reveals that for tests TC010 and TC023 in general, higher numbers as well as higher amounts of large tertiary γ' are present than in the tests TC004 and TC026. Regarding the influence of particle size and dislocation type (weakly and strongly coupled) on the critical resolved shear stress [33], which is necessary to shear the particles, higher critical resolved shear stress evolve for coarse tertiary γ' (closer to 50 μm). Therefore, higher local stresses are necessary for shearing the particles in the test specimen TC010 and TC023. Transferred to stress controlled crack growth TMF tests, the same stress amplitudes were applied to all specimens. But because of the influence on microstructure, less plastic deformation occurs in the plastic zones in front of the crack tips for the specimens TC010 and TC023 which probably leads to lower crack growth rates. For smaller and less tertiary γ' volumes as seen for the microstructures of specimen TC004 and TC026, less shear stresses are required for particle shearing and therefore for plastic deformation. For constant applied stress amplitudes, higher plastic deformation occurs at the crack tip which increases the crack growth. Since the number of secondary γ' is distinctly smaller, shearing of tertiary γ' becomes more probable, especially with regard to the high volume fraction of about 50 %. Therefore, it can be assumed, that the majority of the crack growth behaviour under in-phase TMF tests can be attributed to the tertiary γ' size distribution. It should be noted that these statements are hypothetical and require further examination by considering particle size distributions as well as dislocation movement, by examination via SEM/TEM.

To consider the influence of particle size on the prediction of IP TMF tests, a precipitation size dependent parameter S is developed in order to fit the predictions to the experimental data. A clear separation of the influence of different tertiary γ' sizes distribution on the fatigue as well as on the creep crack growth can't be determined but the provided test data show a clear influence of the size distribution on the total crack growth. As a first approach the current model shown in Figure 9 was used and the parameter S added as multiplier to the total crack growth value. A new optimization procedure was carried out, in order to determine S for every crack growth test with the correlated average tertiary γ' size taken from [25]. Proceeding the results of the optimization, a power law function was fitted for the correlation between average tertiary γ' size and S as Figure 12 demonstrates.

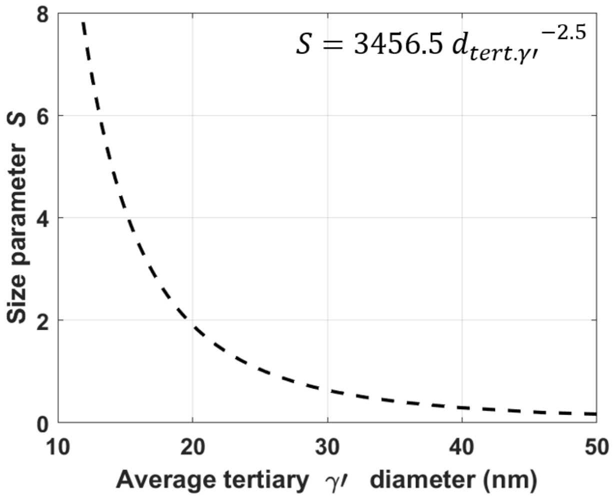

Figure 12: Fitting function in order to determine the parameters S in dependence of the average diameter of the tertiary γ' ($d_{tert.\gamma\prime}$)

It can be seen that minor changes in the precipitation size, especially in the region between 10 nm and 30 nm have a distinct influence on the parameter S. With increasing tertiary γ' size, the influence of S decreases. This relationship is only valid up to an average tertiary γ' size of about 50 nm. With further increase, the particles still count as tertiary γ' (up to 90 nm), but the shearing process changes from weakly to strongly coupled, which results in a different relationship between shear stress and particle size.

The following Figure 13 illustrates the change in crack growth behaviour in dependence of the size dependent parameter S for the four microstructurally investigated tests.

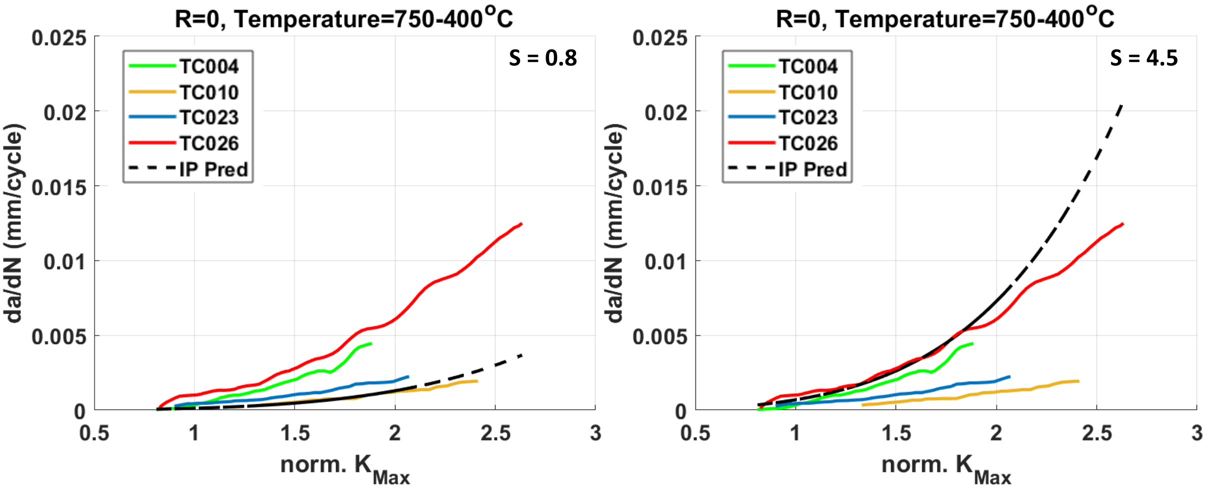

Figure 13: Simulations of the influence of S on the crack growth rate for IP TMF tests, for $S = 0.8$ (left) and $S = 4.5$ (right)

Taking into account the particle size dependent parameter S in the simulation, it is possible to predict the crack growth behaviour for IP TMF test with a good accordance to the experimental results. For further IP tests without microstructural evaluation, the S-value can be determined by further optimization procedures, and the crack growths predicted as Figure 14 illustrates.

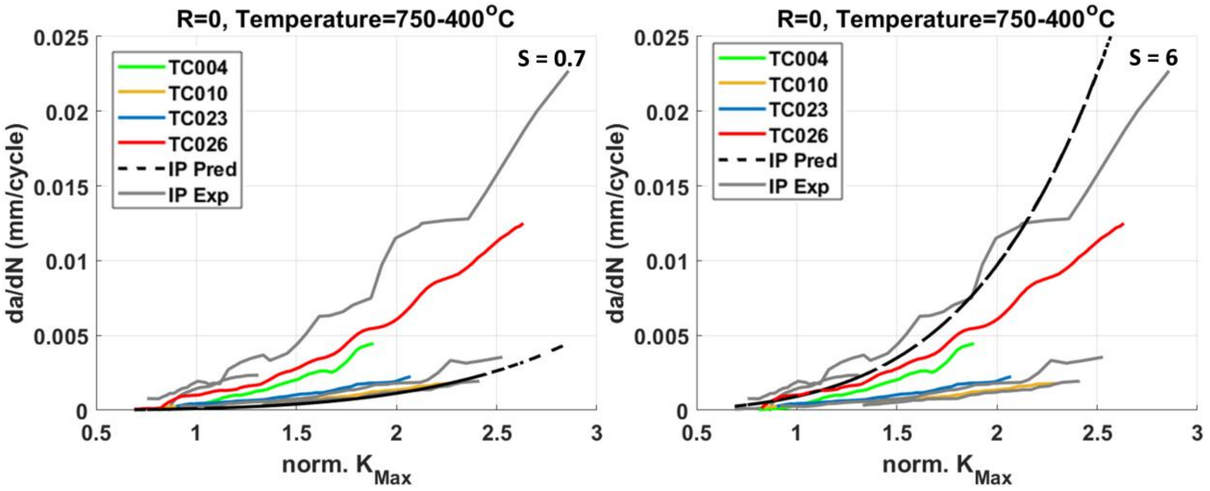

Figure 14: Predicted IP TMF tests using S values determined by optimisation procedures, S = 0.7 covers the lower experimental scatter band (left) and S = 6 the upper experimental scatter band (right)

Since the size influence of S on the crack growth behaviour could be calibrated on the tests shown in Figure 12 and Figure 13, reverse calculation regarding the microstructure can be made. As Figure 14 reveals, the whole scatter band of the experimental results lead to a variation of S between 0.7 and 6 (black dotted line) and enables a prediction of all other conducted IP TMF with no knowledge of the actual microstructural properties (grey lines). Using the mathematical calibrated relationship between S and tertiary γ' (Figure 12), lowest crack growth rates can be found for an average tertiary γ' size of 27.5 μm for $S = 0.7$. However, highest crack growth rates can be found for average tertiary γ' size of 13.7 μm for $S = 6$.

As already mentioned for the OP TMF tests, predictions were in excellent accordance to experimental results, since no distinct scatter in the crack growth behaviour was established. This can be attributed to less sensitivity to microstructural aspects for a temperature of 400 °C at peak load during OP testing, the γ' phase shows distinct higher stiffness compared to the surrounding γ matrix. Therefore, the majority of the plastic deformation occurs in the softer γ matrix. This is particularly characterized by increased dislocation pile up around, as well as dislocation bow out between the particles, according to [31].

4. Conclusions

- Based on the work of Bouvard et al [26] a numerical modelling method was developed to predict the thermo-mechanical long crack growth behaviour of the polycrystalline nickel-base superalloy RR1000.

- In-phase and out-of-phase TMF tests can be predicted with good accordance to experimental results using a unified formulation, based on material parameters deducted from isothermal crack growth test.

- Microstructural observation revealed distinct differences in the size, shape and distribution of secondary γ' and tertiary γ' due to the specimen extraction origin from a turbine component.

- Because of the strong sensitivity of the crack growth to the microstructure during IP testing, a precipitation size dependent parameter $\boldsymbol{S}$ was introduced on the evidence of microstructural investigations. It has been shown that the crack growth rate increases with a decreasing size as well as amount of tertiary γ'. This can be attributed to increased plastic deformation in the area of the crack tip, caused by a decrease of critical resolved shear stress for weakly coupled dislocation to shear the particles. Based on the relationship between the precipitation size and the parameter $\boldsymbol{S}$, predictions about the average particle diameter of tertiary γ' can be concluded but this needs to be verified by further microstructural evaluations.

- OP TMF tests show no sensitivity to microstructural aspects. Since peak load is reached at minimum temperature, plastic deformation primarily occurs in the γ matrix, due to high stiffness differences to the γ' particles. Therefore, no modification of the crack growth rates using $\boldsymbol{S}$ are necessary.
- It should be determined for the precipitation size dependent parameter $\boldsymbol{S}$, for which combinations of temperature and load, deformation behaviour becomes more influenced by the microstructure.
- The model should be extended with a term which considers effects by oxidation. Since the evaluation of oxidation from the given data is not clearly practical, oxidation tests have to be carried out.
- The influence of particle coarsening, especially the tertiary γ' should be investigated. After exceeding a critical size during aging, particles get sheared by strongly coupled dislocations, where the necessary critical shear stress decreases with increasing particles size. For crack growth tests, with high exposure time to high temperatures, a change in slope of crack growth can be expected.

Acknowledgements

This project has received funding from the European Union's Horizon 2020 research and innovation programme and Joint Undertaking Clean Sky 2 under grant agreement No 686600. The authors are also grateful for the supply of material and input from Rolls-Royce plc.

References

[1] Paris P, Erdogan F. A Critical Analysis of Crack Propagation Laws. J. Basic Engineering 1963;85(4):528. https://doi.org/10.1115/1.3656900.

[2] Irwin GR. Analysis of stresses and strains near the end of a crack traversing a plate. Journal of Applied Mechanics 1957:351–69.

[3] Forman RG, Kearney VE, Engle RM. Numerical Analysis of Crack Propagation in Cyclic-Loaded Structures. J. Basic Engineering 1967;89(3):459. https://doi.org/10.1115/1.3609637.

[4] Dubey S, Soboyejo A, Soboyejo W. An investigation of the effects of stress ratio and crack closure on the micromechanisms of fatigue crack growth in. Acta Materialia 1997;45(7):2777–87. https://doi.org/10.1016/S1359-6454(96)00380-1.

[5] Mackay TL, Alperin BJ, Bhatt DD. Near-threshold fatigue crack propagation of several high strength steels. Engineering Fracture Mechanics 1983;18(2):403–16. https://doi.org/10.1016/0013-7944(83)90149-2.

[6] Schmidt RA, Paris PC. Threshold for Fatigue Crack Propagation and the Effects of Load Ratio and Frequency. Progress in Flaw Growth and Fracture Toughness Testing 1973:79–94. https://doi.org/10.1520/STP49638S.

[7] Broek D, Schijve J. The Influence of the Mean Stress on the Propagation of Fatigue Cracks in Light Alloy Sheet. Aircraft Eng & Aerospace Tech 1967;39(3):10–8. https://doi.org/10.1108/eb034240.

[8] Beden SM, Abdullah S, Ariffin AK, Al-Asady NA. Fatigue crack growth simulation of aluminium alloy under spectrum loadings. Materials & Design 2010;31(7):3449–56. https://doi.org/10.1016/j.matdes.2010.01.039.

[9] Cheng A, Chen N-Z. Fatigue crack growth modelling for pipeline carbon steels under gaseous hydrogen conditions. International Journal of Fatigue 2017;96:152–61. https://doi.org/10.1016/j.ijfatigue.2016.11.029.

[10] Tong J, Dalby S, Byrne J, Henderson MB, Hardy MC. Creep, fatigue and oxidation in crack growth in advanced nickel base superalloys. International Journal of Fatigue 2001;23(10):897–902. https://doi.org/10.1016/S0142-1123(01)00049-4.

[11] Kruch S, Prigent P, Chaboche JL. A fracture mechanics based fatigue-creep-environment crack growth model for high temperature. International Journal of Pressure Vessels and Piping 1994;59(1):141–8. https://doi.org/10.1016/0308-0161(94)90149-X.

[12] Wolf E. Fatigue crack closure under cyclic tension. Engineering Fracture Mechanics 1970;2(1):37–45. https://doi.org/10.1016/0013-7944(70)90028-7.

[13] Arana M, Martínez-Esnaola JM, Bressers J. Crack Propagation and Life Prediction in a Nickel-Based Superalloy under TMF Conditions. In: Bressers J, Rémy L, Steen M, Vallés JL, editors. Fatigue under Thermal and Mechanical Loading: Mechanisms, Mechanics and Modelling: Proceedings of the Symposium held at Petten, the Netherlands, 22-24 May 1995. Dordrecht: Springer Netherlands; 1996, p. 393–402.

[14] Minakawa K, McEvily AJ. On crack closure in the near-threshold region. Scripta Metallurgica 1981;15(6):633–6. https://doi.org/10.1016/0036-9748(81)90041-7.

[15] Suresh S, Ritchie RO. A geometric model for fatigue crack closure induced by fracture surface roughness. Metallurgical Transactions A 1982;13(9):1627–31. https://doi.org/10.1007/BF02644803.

[16] Suresh S, Zamiski GF, Ritchie DRO. Oxide-Induced Crack Closure: An Explanation for Near-Threshold Corrosion Fatigue Crack Growth Behavior. Metallurgical and Materials Transactions A 1981;12(8):1435–43. https://doi.org/10.1007/BF02643688.

[17] Skelton P, Haigh J. Fatigue crack growth rates and thresholds in steels under oxidising conditions. Materials Science and Engineering 1978;36(1):17–25. https://doi.org/10.1016/0025-5416(78)90191-X.

[18] Martelo DF, Mateo A, Chapetti MD. Crack closure and fatigue crack growth near threshold of a metastable austenitic stainless steel. International Journal of Fatigue 2015;77:64–77. https://doi.org/10.1016/j.ijfatigue.2015.02.016.

[19] Pippan R, Hohenwarter A. Fatigue crack closure: a review of the physical phenomena. Fatigue & Fracture of Engineering Materials & Structures 2017;40(4):471–95. https://doi.org/10.1111/ffe.12578.

[20] Rice JR. A Path Independent Integral and the Approximate Analysis of Strain Concentration by Notches and Cracks. J. Appl. Mech 1968;35(2):379–86. https://doi.org/10.1115/1.3601206.

[21] Schwalbe KH (ed.). The Crack Tip Opening Displacement in Elastic-Plastic Fracture Mechanics: Proceedings of the Workshop on the CTOD Methodology GKSS-Forschungszentrum Geesthacht, GmbH, Geesthacht, Germany, April 23-25, 1985. Berlin, Heidelberg: Springer Berlin Heidelberg; 1986.

[22] Connor L. The development of a dual microstructure heat treated Ni-base superalloy for turbine disc applications: Ph.D: University of Cambridge.

[23] Jones NG, Christofidou KA, Mignanelli PM, Minshull JP, Hardy MC, Stone HJ. Influence of elevated Co and Ti levels on polycrystalline powder processed Ni-base superalloy. Materials Science and Technology 2014;30(15):1853–61. https://doi.org/10.1179/1743284714Y.0000000509.

[24] Mitchell RJ, Lemsky JA, Ramanathan R, Li HY, Perkins KM, Connor LD. Process Development and Microstructure and Mechanical Property Evaluation of a Dual Microstructure Heat Treated Advanced Nickel Disc Alloy. In: Reed RC, editor. Superalloys 2008: Edited by Roger C. Reed … [et al.]. Warrendale: Tms-Minerals; 2008, p. 347–356.

[25] Jones J, Whittaker M, Lancaster R, Rouse J, Hyde C, Pattison S. The effect of phase angle on crack growth mechanisms under thermo-mechanical fatigue loading. International Journal of Fatigue 2019.

[26] Bouvard J-L, Gallerneau F, Paulmier P, Chaboche JL. A phenomenological model to predict the crack growth in single crystal superalloys at high temperature. International Journal of Fatigue 2012;38. https://doi.org/10.1016/j.ijfatigue.2011.12.011.

[27] Li HY, Sun JF, Hardy MC, Evans HE, Williams SJ, Doel TJA et al. Effects of microstructure on high temperature dwell fatigue crack growth in a coarse grain PM nickel based superalloy. Acta Materialia 2015;90:355–69. https://doi.org/10.1016/j.actamat.2015.02.023.

[28] Grant BMB, Knoche E, Preuss M, da Fonseca JQ, Daymond MR. The Effect of Lattice Misfit on Deformation Mechanisms at High Temperature. AMR 2011;278:144–9. https://doi.org/10.4028/www.scientific.net/AMR.278.144.

[29] Francis EM, Grant BMB, Fonseca JQd, Phillips PJ, Mills MJ, Daymond MR et al. High-temperature deformation mechanisms in a polycrystalline nickel-base superalloy studied by neutron diffraction and electron microscopy. Acta Materialia 2014;74:18–29. https://doi.org/10.1016/j.actamat.2014.04.028.

[30] Stöcker C, Zimmermann M, Christ H-J, Zhan Z-L, Cornet C, Zhao LG et al. Microstructural characterisation and constitutive behaviour of alloy RR1000 under fatigue and creep–fatigue loading conditions. Materials Science and Engineering: A 2009;518(1):27–34. https://doi.org/10.1016/j.msea.2009.04.055.

[31] Knoche E. Influence of the precipitate size on the deformation mechanisms in two nickel-base superalloys [PhD]. Manchster: The University of Manchester; 2011.

[32] Gleiter H, Hornbogen E. Precipitation hardening by coherent particles. Materials Science and Engineering 1968;2(6):285–302. https://doi.org/10.1016/0025-5416(68)90047-5.

[33] Hüther W, Reppich B. Interaction of dislocations with coherent, stress-free ordered particvles 1978(69).

[34] Jackson MP, Reed RC. Heat treatment of UDIMET 720Li: the effect of microstructure on properties. Materials Science and Engineering: A 1999;259(1):85–97. https://doi.org/10.1016/S0921-5093(98)00867-3.

[35] Daymond MR, Preuss M, Clausen B. Evidence of variation in slip mode in a polycrystalline nickel-base superalloy with change in temperature from neutron diffraction strain measurements. Acta Materialia 2007;55(9):3089–102. https://doi.org/10.1016/j.actamat.2007.01.013.

[36] Reppich B, Kühlein W, Meyer G, Puppel D, Schulz M, Schumann G. Duplex γ′ particle hardening of the superalloy Nimonic PE 16. Materials Science and Engineering 1986;83(1):45–63. https://doi.org/10.1016/0025-5416(86)90173-4.

[37] Mitchell RJ, Hardy MC, Preuss M, Tin S. Development of γ;' Morphology in P/M Rotor Disc Alloys During Heat Treatment. In: Superalloys 2004, p. 361–370.